Structural Determinants for the Stereoselective Hydrolysis of Chiral Substrates by Phosphotriesterase[†]

Ping-Chuan Tsai,[§] Yubo Fan,[§] Jungwook Kim,[‖] Lijiang Yang,[§,⊥] Steven C. Almo,*[,‖]
Yi Qin Gao,*[,§,⊥] and Frank M. Raushel*[,§]

[§]*Department of Chemistry, Texas A&M University, College Station, Texas 77843-3255, and* [‖]*Albert Einstein College of Medicine, 1300 Morris Park Avenue, Bronx, New York 10461* [⊥]*Current address: Beijing National Laboratory of Molecular Sciences and College of Chemistry and Molecular Engineering, Peking University, Beijing 100871, China.*

ABSTRACT: Wild-type phosphotriesterase (PTE) preferentially hydrolyzes the R_P enantiomers of the nerve agents sarin (GB) and cyclosarin (GF) and their chromophoric analogues. The active site of PTE can be subdivided into three binding pockets that have been denoted as the small, large, and leaving group pockets based on high-resolution crystal structures. The sizes and shapes of these pockets dictate the substrate specificity and stereoselectivity for catalysis. Mutants of PTE that exhibit substantial changes in substrate specificity and the ability to differentiate between chiral substrates have been prepared. For example, the G60A mutant is stereoselective for the hydrolysis of the R_P enantiomer of the chromophoric analogues of sarin and cyclosarin, whereas the H254G/H257W/L303T (GWT) mutant reverses the stereoselectivity for the enantiomers of these two compounds. Molecular dynamics simulations and high-resolution X-ray structures identified the correlations between structural changes in the active site and the experimentally determined kinetic parameters for substrate hydrolysis. New high-resolution structures were determined for the H257Y/L303T (YT), I106G/F132G/H257Y (GGY), and H254Q/H257F (QF) mutants of PTE. Molecular dynamics calculations were conducted using the S_P and R_P enantiomers of the analogues for sarin and cyclosarin for the wild-type PTE and the G60A, YT, GGY, QF, and GWT mutants. The experimental stereoselectivity correlated nicely with the difference in the computed angle of attack for the nucleophilic hydroxide relative to the phenolic leaving group of the substrate.

Phosphotriesterase (PTE),[1] isolated originally from soil microbes, catalyzes the hydrolysis of a wide range of organophosphate esters, including agricultural insecticides and chemical warfare agents (*1, 2*). The X-ray crystal structure of [Zn^{2+}/Zn^{2+}]PTE reveals a homodimeric $(\beta/\alpha)_8$-barrel structural fold with a binuclear metal center in the active site (*3*). The two zinc ions are bridged by a hydroxide and a carbamate functional group, formed by the reaction of CO_2 with the ε-amino group from an active site lysine residue (*4*). X-ray crystal structures from the Holden laboratory, determined in the presence of inhibitors, have identified three binding pockets that facilitate the association of substrates with the PTE active site (*3*). These subsites have previously been denoted as the small, large, and leaving group pockets and are defined by the space enclosed by the side chains of Gly-60, Ile-106, Leu-303, and Ser-308; side chains of His-254, His-257, Leu-271, and Met-317; and side chains of Trp-131, Phe-132, Phe-306, and Tyr-309, respectively (*3*).

A three-dimensional representation of the PTE active site is presented in Figure 1.

Wild-type PTE is stereoselective for the hydrolysis of chiral organophosphorus esters (*5−8*). The degree of stereoselectivity for the wild-type enzyme depends on the size of the substituents attached to the central phosphorus core. For example, the value of k_{cat}/K_m for wild-type PTE with the R_P enantiomer of compound **1** (a chromophoric analogue of the nerve agent sarin or GB) is 22-fold larger than that for the corresponding S_P enantiomer (*9*). The enantiomeric preference increases to 760 for the hydrolysis of the R_P and S_P enantiomers of compound **2** (an analogue for the nerve agent cyclosarin or GF). The mutation of Gly-60 to alanine results in a substantial enhancement in the relative stereoselectivity for the R_P enantiomers of compounds **1** and **2** (*9*). Rational engineering of PTE, through enlargement of the small pocket and reduction of the large pocket, can invert the inherent enantioselectivity of the wild-type enzyme for the hydrolysis of chiral organophosphonates (*10*). The relative values of k_{cat}/K_m for the R_P and S_P enantiomers of compounds **1** and **2** (Scheme 1) are graphically illustrated in Figure 2 for specific mutants of PTE. Wild-type PTE and the G60A mutant preferentially hydrolyze the R_P enantiomers of compounds **1** and **2** when compared to the corresponding S_P enantiomers, whereas H254G/H257W/L303T (GWT), H257Y/L303T (YT), and I106G/F132G/H257Y (GGY) prefer the S_P enantiomers. The H254Q/H257F (QF) mutant is not stereoselective for the hydrolysis of compound

[1]Abbreviations: PTE, phosphotriesterase; GWT, H254G/H257W/L303T mutant of PTE; YT, H257Y/L303T mutant of PTE; GGY, I106G/F132G/H257Y mutant of PTE; QF, H254Q/H257F mutant of PTE; PDB, Protein Data Bank.
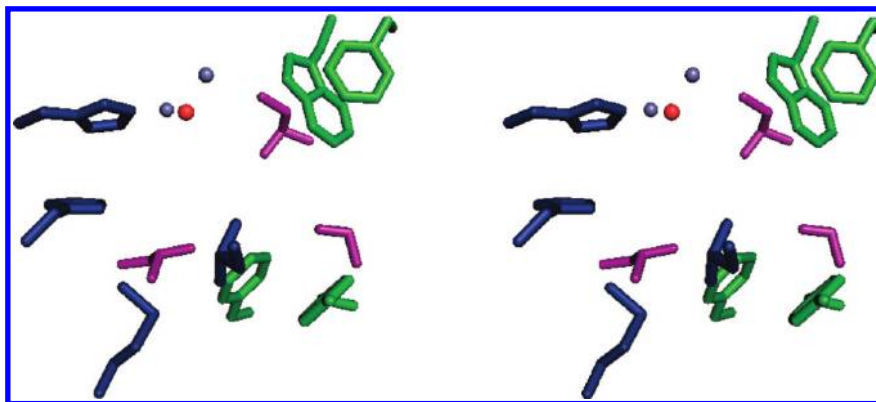
FIGURE 1: Substrate binding pocket of wild-type PTE. The residues assigned to the small, large, and leaving group pockets are colored purple, blue, and green, respectively. The two metal ions are colored light blue, and the bridging hydroxide is colored red. The image was constructed from PDB entry 1HZY.
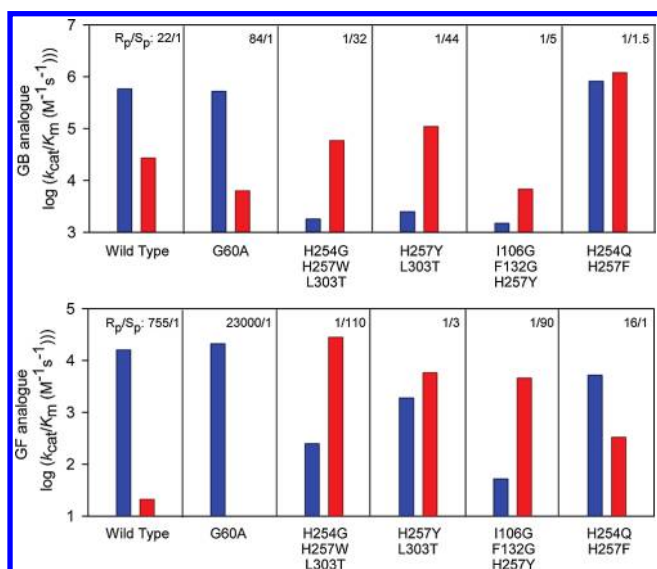

FIGURE 2: Bar graph illustrating the values of k_{cat}/K_m for the R_P and S_P enantiomers of compounds **1** and **2** (*9*).

1, but this mutant enzyme preferentially hydrolyzes the R_P enantiomer of compound **2**.

The stereoselective properties of PTE can be manipulated through the mutation of residues in the active site (*8−11*). What is needed is a physical explanation that is able to correlate changes in the observed kinetic constants with specific changes in the three-dimensional structure. Molecular dynamics simulations have been utilized to probe for correlated changes in three-dimensional structure and catalysis. For example, the wild-type lipase from *Pseudomonas aeruginosa* has no preference for the hydrolysis of either the *R* or *S* enantiomers of 2-methyldecanoic acid esters. However, lipase variants, mutated through directed evolution, were found to have an increased chiral selectivity toward the *S* enantiomer, and molecular dynamics simulations have been conducted on the wild-type and mutant enzymes (*12*). The active site of epoxide hydrolase from *Aspergillus niger* has been redesigned, and the catalytic preference for the *S* enantiomer of glycidyl phenyl ether increased from 5- to 115-fold. The wild-type enzyme and a series of mutant enzymes with enhanced enantioselectivity were investigated using molecular dynamics simulations and molecular docking techniques (*13*).

The X-ray crystal structures of wild-type PTE and five mutants have been determined to high resolution. These structures were

used as the starting point for molecular dynamics simulations with the R_P and S_P enantiomers of compounds **1** and **2** using the AMBER suite of programs. The binding poses of each enantiomer within these proteins support the experimentally observed stereoselectivity for substrate hydrolysis (*9*). These efforts demonstrate that MD simulations can facilitate the design of modified enzymes with enhanced catalytic activities for specific substrates.

MATERIALS AND METHODS

Protein Purification, Crystallization, and X-ray Structure Determination. The QF, GGY, and YT mutants of PTE were expressed and purified to homogeneity as described previously (*8*, *9*). The QF mutant was crystallized by sitting-drop vapor diffusion at 21 °C after mixing 1.0 μL of protein with 1.0 μL of the reservoir solution [0.1 M Bis-Tris (pH 6.5) and 20% PEG MME 5000] and equilibrating over 0.1 mL of the reservoir solution. X-ray data were collected on an R-Axis IV^{++} image plate detector using Cu Kα radiation from a Rigaku RU-H3R X-ray generator and processed using HKL2000 (*14*). The QF crystal exhibited diffraction consistent with space group *P*1. There was a single homodimer of QF in the asymmetric unit. The GGY mutant was crystallized by hanging-drop vapor diffusion at 21 °C by mixing 1.0 μL of protein with 1.0 μL of reservoir solution [0.2 M zinc acetate, 0.1 M sodium cacodylate (pH 6.5), and 12% PEG MME] and equilibrating over 1.0 mL of reservoir solution. X-ray data were collected on the ADSC QUANTUM 210 CCD detector at NSLS beamline X6A. The crystal exhibited diffraction consistent with space group *P*1 with two homodimers in the asymmetric unit. The YT mutant was crystallized by hanging-drop vapor diffusion at 21 °C by mixing 1.0 μL of protein with 1.0 μL of reservoir solution [0.1 M Bis-Tris (pH 6.5) and 12% PEG MME 5000] and equilibrating over 1.0 mL of reservoir solution. X-ray data were collected on the ADSC QUANTUM 315 CCD detector at NSLS beamline X29A. The crystal exhibited diffraction consistent with space group *P*1 with one homodimer in the asymmetric unit.

The structures of the three mutants were determined by molecular replacement using MOLREP with PDB entry 1P6B as the initial search model (*15*). Solvent water molecules were built using Arp/wArp (*16*). All subsequent model building and refinement was conducted with Coot (*17*) and REFMAC5 (*18*) for the QF and GGY mutants or SHELXL (*19*) for the YT mutant. The final models were refined to 1.80, 1.64, and 1.04 Å

Scheme 1: Structures of Organophosphonate Substrates for PTE
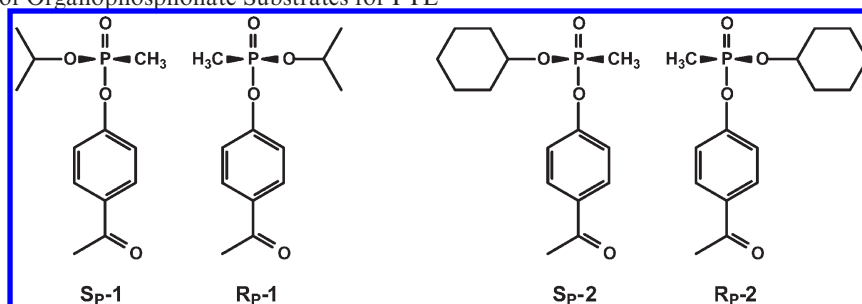
for the QF, GGY, and YT mutants, respectively. The data collection and refinement statistics are listed in Table 1.

Computational Details. Chain A in the X-ray crystal structures of PTE, including the wild-type protein (PDB entry 1EZ2), G60A (PDB entry 3CS2), YT (PDB entry 2OB3), GWT (PDB entry 1P6C), QF (PDB entry 2OQL), and GGY (PDB entry 2O4M), was used for the molecular dynamics simulations with the R_P and S_P enantiomers of **1** and **2** in the active site. The conformations of the amino acid side chains with the highest occupancy were used for the simulations if there were more than one available in the crystal structure. All waters interacting with chain A were kept for the simulations. For the two structures (PDB entries 3CS2 and 2O4M) in which cacodylate was bound in the active site instead of the bridging hydroxide, the active sites were aligned with that of wild-type PTE (PDB entry 1EZ2), the cacodylate was removed, and hydroxide was added between the two Zn^{2+} ions accordingly. The Co^{2+} ions in the active site of G60A in the structure depicted by PDB entry 3CS2 were replaced with Zn^{2+} ions in the computation. The substitution of Co^{2+} in the active site of PTE for Zn^{2+} does not significantly affect the kinetic constants or the overall structure of the active site (*2*). The geometries of the analogues were fully optimized at the level of B3LYP (*20−22*)/6-31++G(d′,p′) (*23−25*), and the charge distribution on each atom in these molecules was computed using the RESP-fit method at the level of B3LYP/cc-pVTZ (*26*) with the solvent effect ($\varepsilon = 4$) included using the polarizable continuum model (PCM) (*27−29*). The force field for Zn^{2+} and the charge distributions for the four Zn-coordinating histidines (His-55, His-57, His-201, and His-230), the carboxylated lysine (Lys-169), and hydroxide were developed by Pang (*30*). The side chains of the Zn-coordinating histidines were fully deprotonated and modeled as imidazolates (*30*). His-254 was assigned as the protonated form, while all of the remaining histidines were kept neutral with N^ε protonated. The aspartate and glutamate residues (Asp-100, Asp-105, Asp-253, and Glu-56) were kept neutral to compensate for the deprotonation of the Zn-coordinating histidines. In the mutant enzymes, the corresponding histidines were kept in the same protonation states as those in the wild-type enzyme except for mutations to His-254 and His-257. The net negative charge was neutralized by added Na^+ ions. Explicit TIP3P waters (*31*) were added as a truncated octahedral water box with a 10 Å buffer.

All operations were processed using the AMBER 9 Leap module (*32*), which led to a total of 72 systems (six enzymes with two chiral substrates and three different initial poses for each enantiomer) solvated with 7400−8000 water molecules. The systems were further extended using the periodic boundary condition. Amber force field 99 (*33*) with the reoptimized parameters for the peptide backbone (*34*) was utilized for all

Table 1: Data Collection and Refinement Statistics for the QF, GGY, and YT Mutants of PTE

	H254Q/ H257F	I106G/F132G/ H257Y	H257Y/ L303T
Data Collection			
space group	*P*1	*P*1	*P*1
cell dimension			
a, b, c (Å)	43.53, 45.37, 79.11	56.76, 68.91, 89.67	43.36, 45.37, 79.21
α, β, γ (deg)	104.75, 93.13, 97.97	90.03, 100.29, 94.12	104.86, 93.27, 97.81
resolution (Å)	50.0−1.80 (1.86−1.80)	50.0−1.58 (1.64−1.58)	50.0−1.04 (1.08−1.04)
I/σ	12.9 (3.0)	10.2 (1.5)	17.3 (6.3)
completeness (%)	91.8 (70.2)	93.1 (73.5)	85.5 (41.4)
redundancy	1.9 (1.8)	1.9 (1.7)	3.4 (2.6)
R_{merge}	0.055 (0.245)	0.075 (0.397)	0.061 (0.188)
Refinement			
no. of observed reflections	49147	155682	235873
no. of protein non-hydrogen atoms	5174	10277	5178
no. of water molecules	700	1636	855
R_{work}	0.146	0.189	0.105
R_{free}	0.189	0.244	0.127
average B factor (Å²)	14.48	19.87	9.99
root-mean-square deviation from ideal geometry			
bond lengths (Å)	0.013	0.016	0.015
bond angles (deg)	1.4	1.6	1.5

amino acid residues and the hydroxide ion, while the general AMBER force field was used for the substrates. MD simulations were conducted at 300 K and 1 atm. The SHAKE algorithm (*35*) was used to constrain all bonds involving hydrogens. A 10.0 Å cutoff was applied for nonbonding interactions. The particle mesh Ewald method was employed to treat the long-range electrostatic interactions (*36, 37*).

MD trajectories were obtained on these structures using the AMBER suite of programs. Two steps of minimization were conducted before MD simulations. During the minimization, the systems were first optimized for 1000 cycles while the backbone of the protein was frozen with a force constant of 500.0 kcal mol^{-1} Å^{-2}. The systems were further optimized for 2500 cycles without restraints, followed by a 20 ps MD simulation of heating the system from 0 to 300 K, with a force constant of 10.0 kcal mol^{-1} Å^{-2} upon all peptide backbone atoms. During the MD simulations, the distance between the oxygen of the P=O moiety and Zn_β was kept at 2.2 Å with a force constant of 100.0 kcal mol^{-1} Å^{-2}. This restraint allows the substrates to interact with the residues in the

three subsites and for the phosphonate core to bind directly to Zn_β prior to hydrolysis. In addition, for many of the disfavored binding states, the substrates would dissociate into the bulk solution in the absence of this restraint because of large unfavorable steric effects. Because the ligands were manually added to the active sites, many disfavored interactions to the protein overwhelmed the binding between the phosphonate core and Zn_β in the initial geometries not only for the favored structures but also for the disfavored ones. Therefore, it would not be possible to compare the disfavored complexes to the more favored states. At a distance (d_{ZnO}) of 2.2 Å, all of the steric effects between the substituents from the substrates are similar to those that would occur prior to hydrolysis, and thus, the overall comparison of the various structures becomes more reasonable. The binding energies computed with this restraint are not very meaningful because the energy contributions from the $Zn_\beta-O$ distance restraint vary for the mutants and the initial binding poses.

In the first nanosecond of relaxation, the O–P–X angle, where O is the oxygen of the bridging hydroxide, P is the phosphorus of the phosphonate ester, and X is one of the three possible singly bonded atoms attached directly to the phosphorus core, was set to 180° with a restraining force constant of 100.0 kcal mol^{-1} deg^{-2}. The restraining force was released after the relaxation. The equilibrium structure without the angle restraint should be similar to the bound substrate complex prior to attack by the bridging hydroxide. The productive conformations in our simulations are close to the near attack conformers (NAC) defined by Bruice (38). The O−P−X angles are defined as A_L, A_A, and A_M, where L, A, and M are the phenolate oxygen in the p-acetophenolate leaving group, the alkoxide oxygen of the isopropyl or cyclohexyl substituent, and the methyl carbon, respectively, for compounds **1** and **2**. The distance between Zn_β and the phosphoryl oxygen of the substrate is defined as d_{ZnO}, while the distance between the phosphorus and the bridging hydroxide oxygen is defined as d_{PO}. Data were collected every 0.5 ps in continuous trajectories until the system reached equilibrium. The lengths of the trajectories varied from 10 to 25 ns. The last 5 ns of the equilibrated trajectories was utilized for structural analyses.

RESULTS AND DISCUSSION

Three-Dimensional Structures of QF, GGY, and YT. The three-dimensional structures of QF, GGY, and YT are nearly identical to that of the wild-type enzyme. In the QF and YT structures, one homodimer was found in the asymmetric unit and two metal atoms are located in the active site, bridged by a water molecule or hydroxide. The crystals of GGY contained two homodimers in the asymmetric unit, but cacodylate is bound between the two active site metal ions instead of hydroxide in all four subunits (data not shown). Cacodylate was included in the crystallization solution, and the binding mode for this compound in the active site is similar to that observed previously in the structure of the G60A mutant (39). Crystals of the YT mutant exhibited outstanding X-ray diffraction; the data were collected and processed to 1.04 Å. The high-resolution data enabled anisotropic temperature factor refinements and yielded a model with R_{work} and R_{free} values of 0.105 and 0.127, respectively. An example of the $2F_o − F_c$ electron density map around the binuclear metal center is shown in Figure 3.

Comparison of Active Site Structures. The active site structures of wild-type PTE and the five mutant enzymes (G60A, YT,
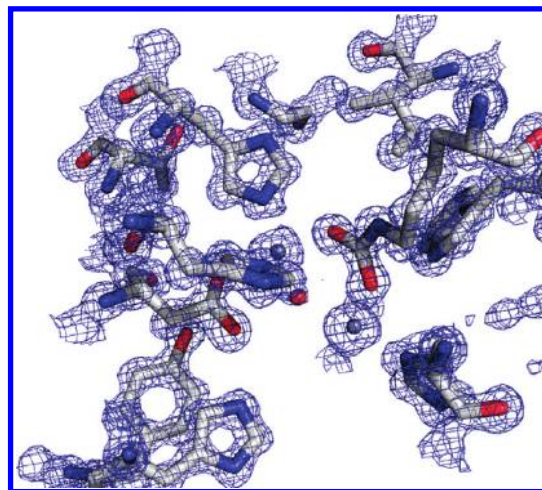

FIGURE 3: $2F_o − F_c$ map of the crystal structure for the YT mutant near the active site at a contour level of 1.5σ. Carbons are colored light gray, nitrogens blue, oxygens red, and arsenics purple. Gray spheres represent zinc.

GWT, QF, and GGY) that have been determined by X-ray crystallography are shown in Figure 4A−F. Superposition of the Cα atoms of the five mutant enzymes with those of wild-type PTE gives root-mean-square deviations for G60A, YT, GWT, GGY, and QF of 0.36, 0.51, 0.42, 0.36, and 0.55 Å, respectively. The mutations that have been introduced into the active site of PTE do not, therefore, significantly change the backbone conformation of the protein, including those regions near the active site. The crystal structures of PTE reveal that the small binding pocket is the most isolated from the external environment compared to the large and leaving group pockets. The large binding pocket is formed by His-254, His-257, Leu-271, and Met-317, but overall, this pocket is accessible to solvent molecules. The leaving group pocket is even more exposed to solvent than the large binding pocket.

The impact of the mutations on the structure of the substrate binding pocket is readily detectable in some instances, as in the structure of GGY (Figure 4C). The replacement of Ile-106 with glycine clearly enlarges the small binding pocket compared to that of the wild-type enzyme, consistent with the observed kinetic results demonstrating that GGY favors the hydrolysis of the S_P enantiomers over the R_P enantiomers. For G60A, the methyl substitution reduced the size of the small binding pocket (Figure 4B), and the preference for the R_P enantiomer is enhanced relative to that of the wild-type enzyme. In some cases, however, the structural changes are somewhat ambiguous, as observed with the H254Q mutation of the QF mutant (Figure 4F). The net effect of the H254G mutation in the GWT mutant is not intuitively clear, because the mutation actually increases the size of the large binding pocket (Figure 4E). The GWT mutant exhibits an inverted stereoselectivity relative to that of the wild-type enzyme and hydrolyzes S_P-**1** and S_P-**2** more effectively than the two R_P enantiomers. The replacement of the adjacent His-257 with tryptophan may have compensated for the changes caused by the H254G mutation.

Mechanism of Action for Substrate Hydrolysis by PTE. A comprehensive reaction mechanism for the hydrolysis of organophosphates by PTE has been proposed (40). In this mechanism, the substrate binds in the active site via an initial interaction of the phosphoryl oxygen with M_β. The bridging hydroxide subsequently attacks the phosphorus center, and the leaving group departs via the formation and/or breakdown of a
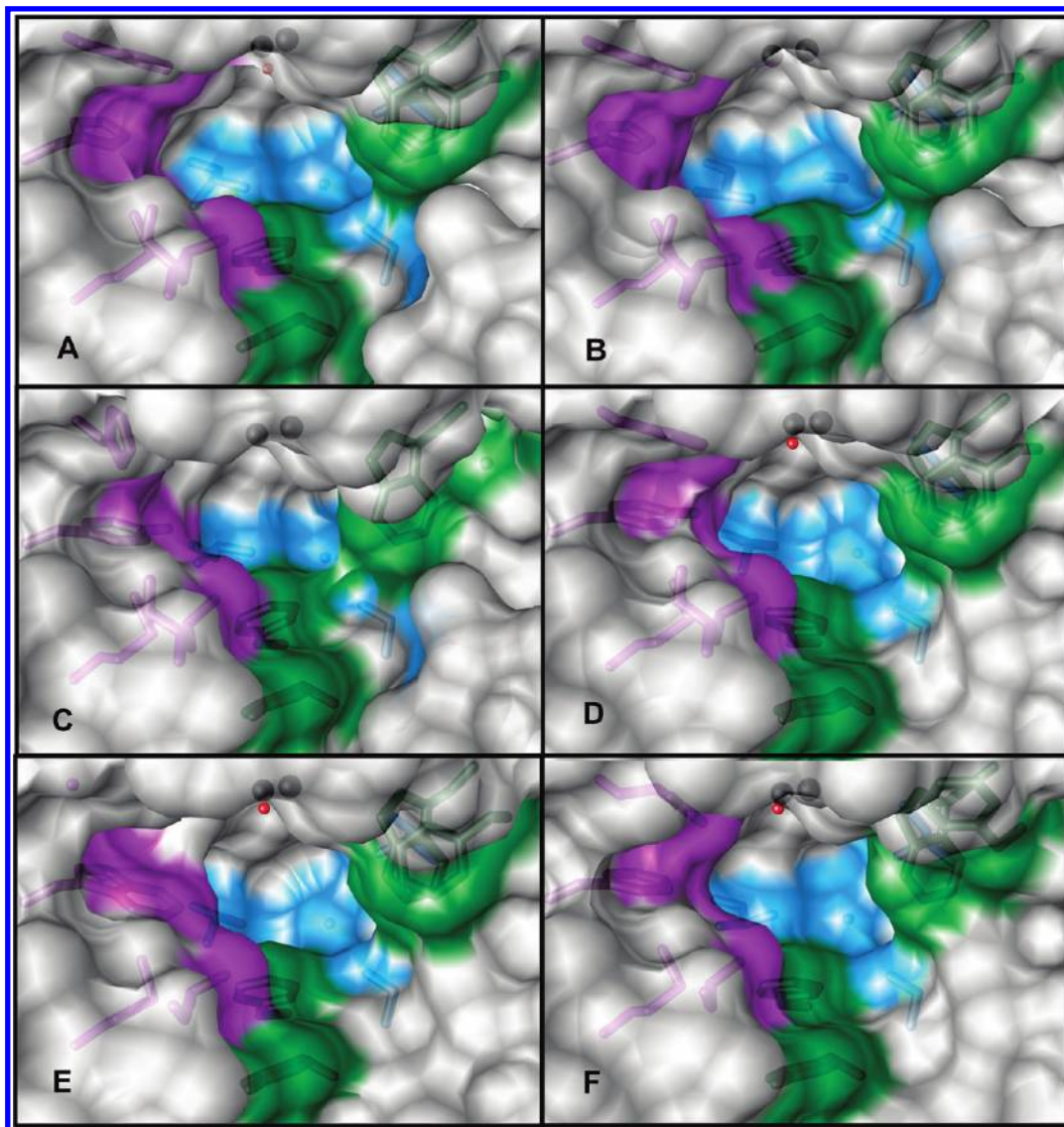
FIGURE 4: Active site structure of wild-type PTE and five mutant enzymes: (A) wild type, (B) G60A, (C) I106G/F132G/H257Y, (D) H257Y/L303T, (E) H254G/H257W/L303T, and (F) H254Q/H257F. The images were drawn with Chimera (*45*, *46*). The surfaces are colored gray; the surfaces for Cα atoms and side chains for residues 254, 257, 317, and 271 are colored purple. The surfaces for residues 60, 303, 308, and 106 are colored blue, and the surfaces for residues 131, 132, 306, and 309 are colored green. The stick figures of the residues are colored a shade darker than their corresponding surfaces. The metals are represented as black spheres, and the bridging water, when present, is shown as a red sphere. A transparency of 15% was placed on the surface with a "one-layer" transparency.

trigonal bipyramidal transition state. This mechanism is consistent with the net inversion of stereochemistry with chiral phosphate substrates (*41*). X-ray crystal structures of bound substrate analogues show that the phosphoryl oxygen electrostatically interacts with M_β (*42*). In addition, the kinetic constants for the hydrolysis of phosphate and thiophosphate esters indicate that the P=O bond is polarized in the transition state by a direct interaction with M_β (*43*). Finally, the three-dimensional structure of diethyl phosphate bound to PTE shows that the hydrolysis product bridges the two divalent cations in the active site and displaces the bridging hydroxide (*39*). On the basis of these experimental observations, the optimal substrate binding pose is one in which the angle of attack by the bridging hydroxide, relative to the leaving group phenol, is ∼180°, and the phosphoryl oxygen is positioned to interact with M_β. In this pose, the angle from the attacking hydroxide to the other two substituents is ∼70° (180° − 110°).

Initial Geometries of Bound Substrates for MD Simulations. Models of the productive binding modes for the R_P and S_P

enantiomers of **1** and **2** with PTE are graphically depicted in Figure 5 and designated as R_L and S_L, respectively. In these initial poses, the phenolate substituent is placed in the leaving group pocket while the methyl and *O*-alkyl groups are positioned in either the small or large pocket, depending on the absolute stereochemistry of the substrate. The four nonproductive binding modes include orientations in which either the methyl or *O*-alkyl group is positioned within the leaving group pocket at an initial angle of ∼180° relative to the attacking hydroxide. These poses have been designated as R_A, R_M, S_A, or S_M, depending on which one of the substituents is positioned within the leaving group pocket. Because compounds **1** and **2** are chiral, there are a total of 12 initial poses for each of the six enzymes to be evaluated.

At the termination of the simulations, the angles from each of the three substituents to the attacking hydroxide and the distances from phosphorus to the hydroxide and from M_β to the phosphoryl oxygen were averaged. The distances (d_{PO} and d_{ZnO}) and angles (A_A, A_L, and A_M) are defined as shown in Scheme 2. A_L represents the angle from the attacking hydroxide
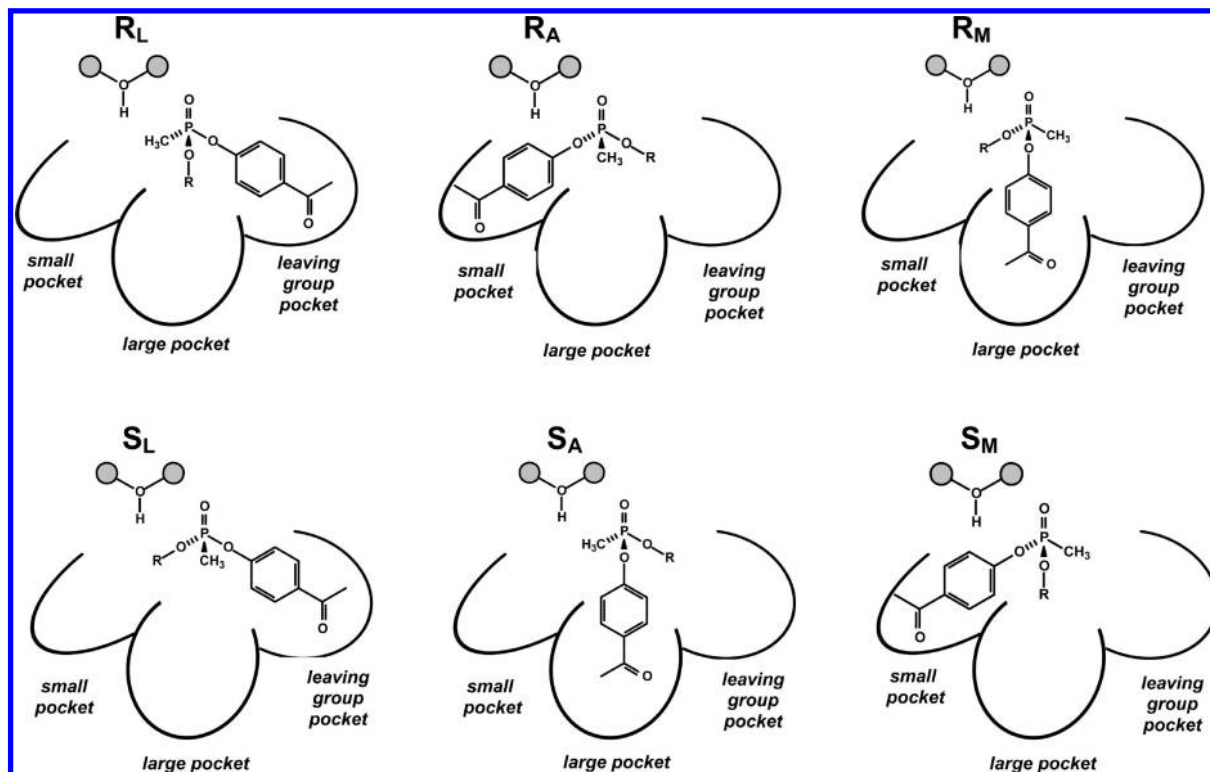
FIGURE 5: Cartoon representations for the initial binding poses for the R_P and S_P enantiomers of compounds **1** and **2** in the active site of PTE. Each enzyme−substrate complex was oriented to have three different initial binding poses during the MD simulations. The binding poses that place the *p*-acetyl phenol group, the O-R group, and the methyl substituent toward the leaving group pocket for the R_P substrate−enzyme complexes are denoted as R_L, R_A, and R_M, respectively. The binding poses that have the *p*-acetyl phenol group, the O-R group, and the methyl substituent toward the leaving group pocket for the S_P substrate−enzyme complex are denoted as S_L, S_A, and S_M, respectively.

Scheme 2: Definition of Angles A_L, A_M, and A_N and Distances d_{PO} and d_{ZO}
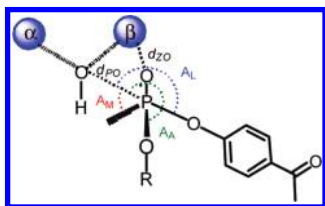
to the leaving group phenol through the phosphorus. A_A is the angle from the hydroxide to the *O*-alkyl group, and A_M is the angle to the methyl substituent. The value of d_{PO} is defined as the distance between the bridging hydroxide and the phosphorus atom of the substrate. The value of d_{ZnO} is the distance between the phosphoryl oxygen and M_β.

The values of A_L for the three initial binding poses for R_P-**1** with wild-type PTE are plotted as a function of time in Figure 6. During the first 1.0 ns, A_L oscillates within a small range because of the initial restraint on this parameter. After 1.0 ns, this restraint was removed and all three substituents within a given substrate were allowed to rotate freely. As shown in Figure 6, the leaving group quickly changes its orientation after the release of the initial restraint. The equilibrium position for each of the starting poses is reached in a relatively short period of time. For the R_L and R_M poses, the relative orientation of the substrate in the active site is quite stable and the phenolic group remains in either the leaving group pocket (for the R_L pose) or large pocket (for the R_M pose). However, for the R_A pose, the leaving group repositions from the small pocket, after the initial restraint is released, to an orientation that is ∼111° relative to the attacking

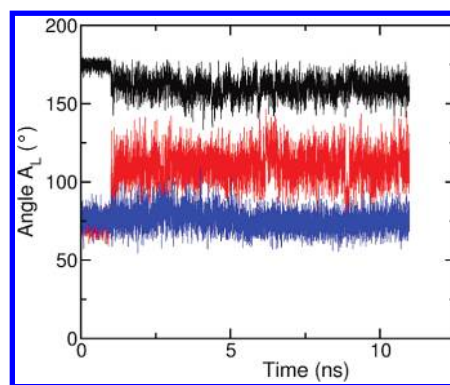FIGURE 6: Changes in the value of the A_L angles for the R_L (black), R_A (red), and R_M (blue) initial binding poses during MD simulation for R_P-**1** with wild-type PTE.

hydroxide. In this structure, the leaving group moves to the large pocket, although the phosphonate core does not rotate significantly relative to the initial geometry. Snapshots selected from the trajectories during the last 5 ns of simulations were used to estimate the average deviations from the initial poses. The angles (A_L) and distances (d_{PO}) in these snapshots were subsequently used to assess the relative reactivities of the various complexes.

Molecular Dynamics Simulations of Wild-Type PTE. The structural parameters for the binding of compounds **1** and **2** to wild-type PTE are listed in Table 2. Representative images of the enzyme−substrate complexes after the MD simulations are shown in panels A and B of Figure 7 for R_P-**1** and S_P-**1** and panels C and D of Figure 7 for R_P-**2** and S_P-**2**, respectively. With R_P-**1**, for the initial pose R_A the leaving group is not in an appropriate orientation relative to the attacking hydroxide with an A_L value

Table 2: Structural Parameters for the Complexes between Wild-Type PTE and the R_P and S_P Enantiomers of **1** and **2**

| substrate	parameter	initial pose					
		R_L	R_A	R_M	S_L	S_A	S_M
compound **1**	A_L	160 ± 6	111 ± 10	74 ± 6	140 ± 6	68 ± 5	142 ± 9
	A_A	70 ± 5	137 ± 10	96 ± 4	90 ± 11	160 ± 8	104 ± 10
	A_M	95 ± 7	70 ± 5	164 ± 5	98 ± 16	90 ± 7	75 ± 7
	d_{PO}	3.4 ± 0.1	3.5 ± 0.1	3.6 ± 0.1	3.8 ± 0.2	3.4 ± 0.1	3.6 ± 0.2
	d_{ZnO}	2.1 ± 0.1	2.1 ± 0.1	2.1 ± 0.1	2.1 ± 0.1	2.1 ± 0.1	2.1 ± 0.1
compound **2**	A_L	156 ± 6	75 ± 7	108 ± 8	143 ± 8	64 ± 6	95 ± 6
	A_A	67 ± 6	159 ± 7	78 ± 4	101 ± 9	149 ± 6	94 ± 4
	A_M	100 ± 7	87 ± 8	146 ± 7	80 ± 8	110 ± 7	148 ± 5
	d_{PO}	3.5 ± 0.1	3.4 ± 0.2	3.8 ± 0.1	3.8 ± 0.2	3.6 ± 0.2	4.0 ± 0.1
	d_{ZnO}	2.1 ± 0.1	2.1 ± 0.1	2.1 ± 0.1	2.1 ± 0.1	2.1 ± 0.1	2.1 ± 0.1
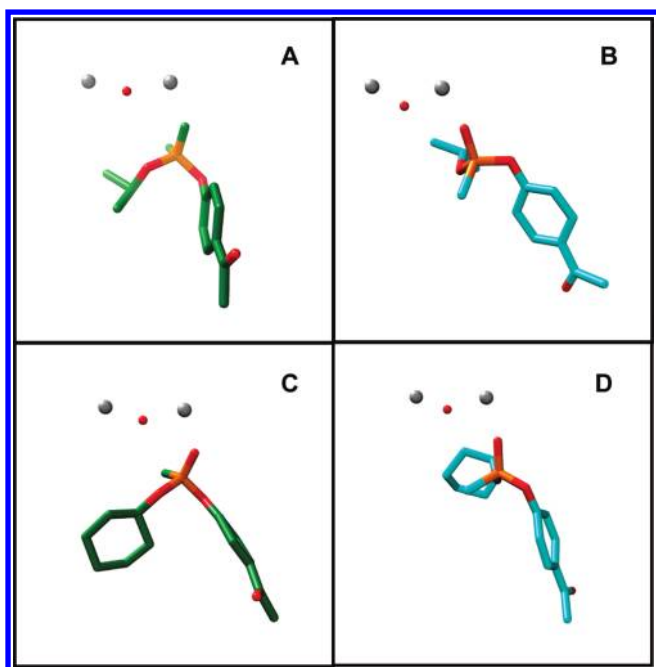
FIGURE 7: Orientation of the R_P and S_P enantiomers of compounds **1** and **2** with wild-type PTE determined from the MD simulations. (A) R_L for compound **1**. (B) S_L posed for compound **1**. (C) R_L posed for compound **2**. (D) S_L pose for compound **2**.

of 111°, and thus, displacement of the leaving group cannot readily occur. From the three initial binding complexes, R_L has the best final orientation with an A_L value of 160°, which is the closest to 180° among the values of all the poses. In R_A and R_M, the leaving group is unproductively positioned at 111° and 74°, respectively. In addition, the distance between the bridging hydroxide and phosphorus, d_{PO}, is the shortest for A_L, with a value of 3.4 Å. Therefore, the initial binding pose of R_L is the most optimal in leading to productive hydrolysis of R_P-**1**.

The equilibrium orientation of the leaving group starting from S_A is not in an appropriate position for hydrolysis with an A_L value of 68°. For either S_L or S_M, the equilibrium value for A_L is ~140–142°, which deviates from the ideal angle of ~180°. Because the bulky phenolate group is too large to fit properly in the small binding pocket, a conformational change was observed in the MD simulations for S_M. The phenolate group rotates out of the small binding pocket and forms a complex in the active site in a binding mode that is very similar to S_L, although not identical. These results are consistent with the higher reactivity of wild-type PTE for R_P-**1** relative to S_P-**1**.

The attack angle (161° vs 140°) and shorter distance (3.4 Å) between the hydroxide and phosphorus (3.8 Å) favors R_L over S_L, and thus, the R_P enantiomer of **1** is a better substrate than the S_P enantiomer.

For the R_P and S_P enantiomers of **2**, the equilibrium value of A_L (156°) for R_L is greater than that for S_L (143°) and the distance between hydroxide and the phosphorus center (d_{PO}) is shorter by 0.3 Å (3.5 Å vs 3.8 Å). Therefore, the values for A_L and d_{PO} are more optimal for the hydrolysis of R_P-**2** than for S_P-**2** for an in-line S_N2-like reaction mechanism. In the MD simulations, the conformational change from S_M to S_L was not observed in the analysis of S_P-**2**. The larger size of the cyclohexyl group over the isopropyl group apparently prevents the S_M conformation from rotating to an S_L-like conformation during the simulation.

Molecular Dynamics Simulations with the G60A Mutant. During the simulations, the initial R_A pose changes to an R_L-like one because of the enhanced mismatch of the bulky leaving group and the reduced size of the small pocket. For the R_L and S_L poses, the angle A_L for the R_P enantiomer is greater than that for the S_P enantiomer by 40° (Table 3). The distance d_{PO} for the R_P enantiomer is shorter than that for the S_P enantiomer by 0.6 Å. These results are fully consistent with the observed enhancement in the ratio of hydrolysis of the R_P and S_P enantiomers relative to that of the wild-type enzyme. G60A catalyzes the hydrolysis of the R_P enantiomer 84-fold faster than the S_P enantiomer.

For compound **2**, the initial R_L pose is the only one that results in a suitable angle of attack A_L (162°) for the bridging hydroxide (Table 4). In addition, the distance (d_{PO}) between the bridging hydroxide and the phosphorus center is the shortest for this pose. The A_L angles for the five other initial poses are all smaller than 103° (see Tables S1–S5 of the Supporting Information). The reduced small pocket strongly disfavors the binding of either the *p*-acetylphenol leaving group or the cyclohexyl substituent. Because of steric repulsion between the cyclohexyl group and the small pocket, the initial S_L pose changes to the S_A pose during the MD simulation. The large difference in the computed value of A_L for R_L relative to S_L (84°) is consistent with the substantial difference in rates for the hydrolysis of the R_P and S_P enantiomers of compound **2** by the G60A mutant.

Molecular Dynamics Simulations with GWT, YT, and GGY. The GWT, YT and GGY mutants favor the hydrolysis of the S_P enantiomer of compound **1**. The stereoselectivity of these mutants is thus inverted relative to that of the wild-type enzyme. Consistent with these results, the computed values for ΔA_L-(R_P–S_P) with compound **1** are reversed relative to those of wild-type PTE, although the values (−2, −6, and 0 for GWT, YT, and

Table 3: Comparison of the Attack Angle, A_L, and the Distance, d_{ZnO}, for the Productive Binding Poses of **1** with Wild-Type PTE and Five Mutants

	wild type	G60A	H254G/H257W/L303T	H257Y/L303T	I106G/F132G/H257Y	H254Q/H257F
R_P/S_P ratio	22	84	1/33	1/44	1/5	1/1.5
A_L (deg)						
R_P	160 ± 6	163 ± 7	148 ± 9	146 ± 9	150 ± 5	155 ± 7
S_P	140 ± 6	123 ± 14	150 ± 8	152 ± 6	150 ± 9	147 ± 9
$\Delta A_L(R_P-S_P)$ (deg)	20 ± 6	40 ± 14	-2 ± 9	-6 ± 9	0 ± 9	8 ± 9
d_{PO} (Å)						
R_P	3.4 ± 0.1	3.4 ± 0.1	3.8 ± 0.2	3.9 ± 0.2	3.5 ± 0.1	3.6 ± 0.2
S_P	3.8 ± 0.2	3.9 ± 0.1	3.6 ± 0.2	3.6 ± 0.1	3.6 ± 0.1	3.7 ± 0.2
$\Delta d_{PO}(R_P-S_P)$ (Å)	-0.4 ± 0.2	-0.5 ± 0.1	0.2 ± 0.2	0.3 ± 0.2	-0.08 ± 0.1	-0.12 ± 0.2

Table 4: Comparison of Attack Angle A_L and Distance d_{ZnO} for the Productive Binding Poses of **2** with Wild-Type PTE and Five Mutants.

	wide type	G60A	H254G/H257W/L303T	H257Y/L303T	I106G/F132G/H257Y	H254Q/H257G
R_P/S_P ratio	755	23000	1/110	1/3	1/90	16
A_L (deg)						
R_P	156 ± 6	162 ± 5	151 ± 12	150 ± 8	130 ± 9	166 ± 5
S_P	143 ± 8	78 ± 12	149 ± 8	152 ± 5	144 ± 8	150 ± 5
$\Delta A_L(R_P-S_P)$ (deg)	13 ± 8	84 ± 12	2 ± 12	-2 ± 8	-14 ± 9	16 ± 5
d_{PO} (Å)						
R_P	3.5 ± 0.1	3.4 ± 0.1	3.5 ± 0.2	3.8 ± 0.2	4.2 ± 0.2	3.3 ± 0.1
S_P	3.8 ± 0.2	3.6 ± 0.2	3.8 ± 0.2	3.7 ± 0.1	3.8 ± 0.2	3.8 ± 0.1
$\Delta d_{PO}(R_P-S_P)$ (Å)	-0.3 ± 0.2	-0.2 ± 0.2	-0.3 ± 0.2	0.1 ± 0.2	0.4 ± 0.2	-0.5 ± 0.1

GGY, respectively) are not significantly different from one another given the computational uncertainties associated with these values (Table 3). For the GWT and YT mutants, the values of d_{PO} for the S_P enantiomer are shorter than those for the R_P enantiomer by 0.2 and 0.3 Å, respectively. However, Δd_{PO}-(R_P-S_P) for the GGY mutant is essentially zero.

The GGY, YT, and GWT mutants prefer to hydrolyze the S_P enantiomer of compound **2**. The values for $\Delta A_L(R_P-S_P)$ with GGY and YT are $-14°$ and $-2°$, respectively. Moreover, d_{PO} for the S_P enantiomers is 0.4 Å shorter for the GGY mutant and 0.1 Å shorter for the YT mutant (Table 4). However, for the GWT mutant, these two parameters favor the R_P enantiomer by 2° and 0.3 Å, respectively.

Molecular Dynamics Simulations with QF. No significant stereoselectivity toward compound **1** was observed for QF. However, this mutant preferably hydrolyzes the R_P enantiomer of compound **2**, relative to the S_P enantiomer by a factor of 16 . From the simulations with compound **1** bound to QF, small differences were found for both $\Delta A_L(R_P-S_P)$ and $\Delta d_{PO}(R_P-S_P)$ of 8° and -0.1 Å, respectively. However, for compound **2**, a favored $\Delta A_L(R_P-S_P)$ of 16° and a $\Delta d_{PO}(R_P-S_P)$ of -0.5 Å for the R_P enantiomer were obtained (Table 4).

Correlation between A_L and Reactivity. The analysis of the MD results has focused on the attack angle (A_L) and the distance between the hydroxide and the phosphorus center of the substrate (d_{PO}). The strongest correlation with the observed stereoselectivity is attack angle A_L. Shown in Figure 8 is a plot of the relative reactivity for hydrolysis of the two enantiomers of compounds **1** and **2** with the value of $\Delta A_L(R_P-S_P)$, where the maximum possible value for $\Delta A_L(R_P-S_P)$ is ~110°. The largest deviations from this correlation occur for the hydrolysis of compound **2** with the wild type and the GWT mutant. For compound **2**, the bulky cyclohexyl group complicates the interactions between the substrate and the active site. Therefore, the conformational degrees of freedom are likely to be more complex and may involve concerted motions of substrate and nearby
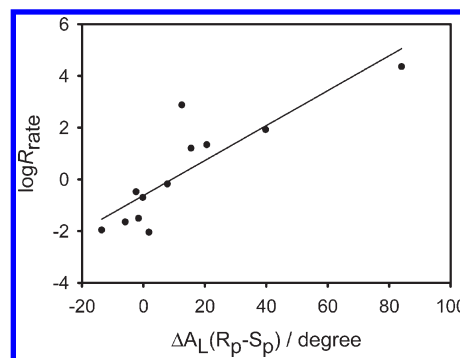
FIGURE 8: Correlation between the experimental logarithm of $(k_{cat}/K_m)_R/(k_{cat}/K_m)_S$ and $\Delta A_L(R_P-S_P)$.

residues. The overall efficiency of hydrolysis of compound **2** is significantly lower than that of compound **1** (as judged by the absolute value of k_{cat}/K_m), indicating that the size of the cyclohexyl group might be too large to fit optimally in the active site.

The values of $\Delta d_{PO}(R_P-S_P)$ are not directly related to the chiral preferences observed experimentally but appear to be a consequence of $\Delta A_L(R_P-S_P)$, resulting in an enhancement in selectivity. For compound **1**, the more optimal the value of A_L, the smaller the value of d_{PO}. However, this relationship does not hold for compound **2**.

Summary. Wild-type PTE preferentially hydrolyzes the less toxic R_P enantiomers of the nerve agents GB and GF (*9*) and the chromophoric analogues (compounds **1** and **2**) of these nerve agents. Mutations localized to the active site of PTE in which the stereoselectivity is either enhanced or inverted have been identified (*8, 9, 11*). It has been assumed that the enhancement in reactivity for the hydrolysis of the initially slower S_P enantiomers is derived from the optimization of the active site for the specific compound to be hydrolyzed. For example, the methyl and isopropyl groups in the R_P enantiomer of compound **1** fit reasonably well in the small and large pockets when the phosphoryl

oxygen interacts with Zn_β and the leaving group points outward toward solution. Because the S_P enantiomer of compound **1** is turned over at a rate that is $^1/_{20}$ of that of the R_P enantiomer, the orientation and/or conformational dynamics of PTE bound with S_P-**1** must be inferior to that for R_P-**1**. The relatively straightforward strategy of resizing the large and small pockets using rational design and semirandom mutagenesis achieved the desired results in the enhancement or inversion of stereoselectivity exhibited by the wild-type enzyme (*8*, *10*, *11*, *44*). The G60A mutant suppresses the rate of hydrolysis of the slow S_P enantiomers of **1** and **2** through the substitution of a methyl group into the small pocket within the active site. In the GWT mutant, the stereoselectivity is apparently reversed by reducing the size of the large pocket and expanding the size of the small pocket.

On the basis of the MD simulations, the orientation of the leaving group is the determining factor for chiral selectivity. The optimization of the substrate within the active site can be estimated by the angle of the attacking hydroxide toward the phosphorus center relative to the leaving group phenol. A direct correlation was found for the experimentally determined stereoselectivity and the calculated attack angle (Figure 8). For these compounds, the stereoselectivity varies over a range of 6 orders of magnitude. The logarithm of $^{R/S}(k_{cat}/K_m)$ correlates positively with the difference in the angle of attack on the phosphorus center by the bridging hydroxide, $\Delta A_L(R_P - S_P)$. The correlation was superior for the enantiomers of **1** relative to **2**, which implies that the more bulky cyclohexyl substituent in **2** may induce some more complex binding interactions. To address these issues, longer time scale simulations based on enhanced sampling techniques and additional initial binding poses can be tested.

ACKNOWLEDGMENT

SUPPORTING INFORMATION AVAILABLE

MD simulations for the G60A, H257Y/L303T, H254G/H257W/L303T, and I106G/F132G/H257Y mutants (Tables S1–S5). This material is available free of charge via the Internet at http://pubs.acs.org.

REFERENCES

1. Dumas, D. P., Durst, H. D., Landis, W. G., Raushel, F. M., and Wild, J. R. (1990) Inactivation of organophosphorus nerve agents by the phosphotriesterase from *Pseudomonas diminuta. Arch. Biochem. Biophys. 277*, 155–159.

2. Omburo, G. A., Kuo, J. M., Mullins, L. S., and Raushel, F. M. (1992) Characterization of the zinc binding site of bacterial phosphotriesterase. *J. Biol. Chem. 267*, 13278–13283.

3. Benning, M. M., Hong, S. B., Raushel, F. M., and Holden, H. M. (2000) The binding of substrate analogs to phosphotriesterase. *J. Biol. Chem. 275*, 30556–30560.

4. Benning, M. M., Kuo, J. M., Raushel, F. M., and Holden, H. M. (1994) Three-dimensional structure of phosphotriesterase: An enzyme capable of detoxifying organophosphate nerve agents. *Biochemistry 33*, 15001–15007.

5. Hong, S. B., and Raushel, F. M. (1999) Stereochemical preferences for chiral substrates by the bacterial phosphotriesterase. *Chem.-Biol. Interact. 120*, 225–234.

6. Chen-Goodspeed, M., Sogorb, M., and Raushel, F. M. (1999) Determining reactivity and stereospecificity of phosphotriesterase from *Pseudonomas diminuta* by site-specific mutagenesis. *FASEB J. 13*, A1446–A1446.

7. Chen-Goodspeed, M., Sogorb, M. A., Wu, F. Y., Hong, S. B., and Raushel, F. M. (2001) Structural determinants of the substrate and stereochemical specificity of phosphotriesterase. *Biochemistry 40*, 1325–1331.

8. Chen-Goodspeed, M., Sogorb, M. A., Wu, F. Y., and Raushel, F. M. (2001) Enhancement, relaxation, and reversal of the stereoselectivity for phosphotriesterase by rational evolution of active site residues. *Biochemistry 40*, 1332–1339.

9. Tsai, P. C., Bigley, A., Li, Y., Ghanem, E., Cadieux, C. L., Kasten, S. A., Reeves, T. E., Cerasoli, D. M., and Raushel, F. M. (2010) Stereoselective hydrolysis of organophosphate nerve agents by the bacterial phosphotriesterase. *Biochemistry 49*, (preceding paper in this issue).

10. Hill, C. M., Li, W. S., Thoden, J. B., Holden, H. M., and Raushel, F. M. (2003) Enhanced degradation of chemical warfare agents through molecular engineering of the phosphotriesterase active site. *J. Am. Chem. Soc. 125*, 8990–8991.

11. Li, W. S., Lum, K. T., Chen-Goodspeed, M., Sogorb, M. A., and Raushel, F. M. (2001) Stereoselective detoxification of chiral sarin and soman analogues by phosphotriesterase. *Bioorg. Med. Chem. 9*, 2083–2091.

12. Bocola, M., Otte, N., Jaeger, K. E., Reetz, M. T., and Thiel, W. (2004) Learning from directed evolution: Theoretical investigations into cooperative mutations in lipase enantioselectivity. *ChemBioChem 5*, 214–223.

13. Reetz, M. T., Bocola, M., Wang, L. W., Sanchis, J., Cronin, A., Arand, M., Zou, J., Archelas, A., Bottalla, A. L., Naworyta, A., and Mowbray, S. L. (2009) Directed evolution of an enantioselective epoxide hydrolase: Uncovering the source of enantioselectivity at each evolutionary stage. *J. Am. Chem. Soc. 131*, 7334–7343.

14. Otwinowski, Z., and Minor, W. (1997) Macromolecular Crystallography, Part A. Methods in Enzymology (Carter, C. W., Jr., and Sweet, R. M., Eds.) pp 307−326, Academic Press, San Diego.

15. Vagin, A., and Teplyakov, A. (1997) MOLREP: An automated program for molecular replacement. *J. Appl. Crystallogr. 30*, 1022–1025.

16. Lamzin, V. S., Wilson, K. S., and Perrakis, A. (2001) Crystallography of biological macromolecules. In International Tables for Crystallography (Rossmann, M. G., and Arnold, E., Eds.) pp 720−722, Kluwer Academic Publishers, Dordrecht, The Netherlands.

17. Emsley, P., and Cowtan, K. (2004) Coot: Model-building tools for molecular graphics. *Acta Crystallogr. D60*, 2126–2132.

18. Murshudov, G. N., Vagin, A. A., and Dodson, E. J. (1997) Refinement of macromolecular structures by the maximum-likelihood method. *Acta Crystallogr. D53*, 240–255.

19. Sheldrick, G. M., and Schneider, T. R. (1997) SHELXL: High-resolution refinement. *Methods Enzymol. 277*, 319–343.

20. Becke, A. D. (1988) Density-Functional Exchange-Energy Approximation with Correct Asymptotic-Behavior. *Phys. Rev. A 38*, 3098–3100.

21. Becke, A. D. (1993) A New Mixing of Hartree-Fock and Local Density-Functional Theories. *J. Chem. Phys. 98*, 1372–1377.

22. Lee, C. T., Yang, W. T., and Parr, R. G. (1988) Development of the Colle-Salvetti Correlation-Energy Formula into a Functional of the Electron-Density. *Phys. Rev. B 37*, 785–789.

23. Krishnan, R., Binkley, J. S., Seeger, R., and Pople, J. A. (1980) Self-Consistent Molecular-Orbital Methods. 20. Basis Set for Correlated Wave-Functions. *J. Chem. Phys. 72*, 650–654.

24. Clark, T., Chandrasekhar, J., Spitznagel, G. W., and Schleyer, P. V. (1983) Efficient Diffuse Function-Augmented Basis-Sets for Anion Calculations. 3. The 3-21+G Basis Set for 1st-Row Elements, Li-F. *J. Comput. Chem. 4*, 294–301.

25. Hehre, W. J., Ditchfie, R, and Pople, J. A. (1972) Self-Consistent Molecular-Orbital Methods. 12. Further Extensions of Gaussian-Type Basis Sets for Use in Molecular-Orbital Studies of Organic-Molecules. *J. Chem. Phys. 56*, 2257–2261.

26. Kendall, R. A., Dunning, T. H., and Harrison, R. J. (1992) Electron-Affinities of the 1st-Row Atoms Revisited: Systematic Basis-Sets and Wave-Functions. *J. Chem. Phys. 96*, 6796–6806.

27. Cances, E., Mennucci, B., and Tomasi, J. (1997) A new integral equation formalism for the polarizable continuum model: Theoretical background and applications to isotropic and anisotropic dielectrics. *J. Chem. Phys. 107*, 3032–3041.

28. Cossi, M., Barone, V., Mennucci, B., and Tomasi, J. (1998) Ab initio study of ionic solutions by a polarizable continuum dielectric model. *Chem. Phys. Lett. 286*, 253–260.

29. Mennucci, B., Cances, E., and Tomasi, J. (1997) Evaluation of solvent effects in isotropic and anisotropic dielectrics and in ionic solutions with a unified integral equation method: Theoretical bases, computational

implementation, and numerical applications. *J. Phys. Chem. B 101*, 10506–10517.

30. Pang, Y. P. (2001) Successful molecular dynamics simulation of two zinc complexes bridged by a hydroxide in phosphotriesterase using the cationic dummy atom method. *Proteins 45*, 183–189.

31. Jorgensen, W. L., Chandrasekhar, J., Madura, J. D., Impey, R. W., and Klein, M. L. (1983) Comparison of Simple Potential Functions for Simulating Liquid Water. *J. Chem. Phys. 79*, 926–935.

32. Case, D. A., Darden, T. A., Cheatham, T. E., III, Simmerling, C. L., Wang, J., Duke, R. E., Luo, R., Merz, K. M., Pearlman, D. A., Crowley, M., Walker, R. C., Zhang, W., Wang, B., Hayik, S., Roitberg, A., Seabra, G., Wong, K. F., Paesani, F., Wu, X., Brozell, S., Tsui, V., Gohlke, H., Yang, L., Tan, C., Mongan, J., Hornak, V., Cui, G., Beroza, P., Mathews, D. H., Schafmeister, C., Ross, W. S., and Kollman, P. A. (2006) AMBER 9, University of California, San Francisco.

33. Wang, J. M., Cieplak, P., and Kollman, P. A. (2000) How well does a restrained electrostatic potential (RESP) model perform in calculating conformational energies of organic and biological molecules? *J. Comput. Chem. 21*, 1049–1074.

34. Simmerling, C., Strockbine, B., and Roitberg, A. E. (2002) All-atom structure prediction and folding simulations of a stable protein. *J. Am. Chem. Soc. 124*, 11258–11259.

35. van Gunsteren, W. F., and Berendsen, H. J. C. (1977) Algorithms for Macromolecular Dynamics and Constraint Dynamics. *Mol. Phys. 34*, 1311–1327.

36. Darden, T., York, D., and Pedersen, L. (1993) Particle Mesh Ewald: An N.Log(N) Method for Ewald Sums in Large Systems. *J. Chem. Phys. 98*, 10089–10092.

37. Essmann, U., Perera, L., Berkowitz, M. L., Darden, T., Lee, H., and Pedersen, L. G. (1995) A Smooth Particle Mesh Ewald Method. *J. Chem. Phys. 103*, 8577–8593.

38. Bruice, T. C. (2002) A view at the millennium: The efficiency of enzymatic catalysis. *Acc. Chem. Res. 35*, 139–148.

39. Kim, J., Tsai, P. C., Chen, S. L., Himo, F., Almo, S. C., and Raushel, F. M. (2008) Structure of diethyl phosphate bound to the binuclear metal center of phosphotriesterase. *Biochemistry 47*, 9497–9504.

40. Aubert, S. D., Li, Y. C., and Raushel, F. M. (2004) Mechanism for the hydrolysis of organophosphates by the bacterial phosphotriesterase. *Biochemistry 43*, 5707–5715.

41. Lewis, V. E., Donarski, W. J., Wild, J. R., and Raushel, F. M. (1988) Mechanism and Stereochemical Course at Phosphorus of the Reaction Catalyzed by a Bacterial Phosphotriesterase. *Biochemistry 27*, 1591–1597.

42. Benning, M. M., Hong, S. B., Raushel, F. M., and Holden, H. M. (2000) The binding of substrate analogs to phosphotriesterase. *J. Biol. Chem. 275*, 30556–30560.

43. Raushel, F. M. (2002) Bacterial detoxification of organophosphate nerve agents. *Curr. Opin. Microbiol. 5*, 288–295.

44. Lum, K. T. (2004) Directed evolution of phosphotriesterase: Towards the efficient detoxification of sarin and soman. Ph.D. Dissertation, Department of Toxicology, Texas A&M University, College Station, TX.

45. Pettersen, E. F., Goddard, T. D., Huang, C. C., Couch, G. S., Greenblatt, D. M., Meng, E. C., and Ferrin, T. E. (2004) UCSF Chimera: A visualization system for exploratory research and analysis. *J. Comput. Chem. 25*, 1605–1612.

46. Couch, G. S., Hendrix, D. K., and Ferrin, T. E. (2006) Nucleic acid visualization with UCSF Chimera. *Nucleic Acids Res. 34*, e29.